

# Reverse-time migration using the Poynting vector

Kwangjin Yoon<sup>1</sup> Kurt J. Marfurt<sup>2</sup>

**Key Words:** Wave equation migration, Reverse-time, Poynting vector, Common image gather

## ABSTRACT

Recently, rapid developments in computer hardware have enabled reverse-time migration to be applied to various production imaging problems. As a wave-equation technique using the two-way wave equation, reverse-time migration can handle not only multi-path arrivals but also steep dips and overturned reflections. However, reverse-time migration causes unwanted artefacts, which arise from the two-way characteristics of the hyperbolic wave equation. Zero-lag cross correlation with diving waves, head waves and back-scattered waves result in spurious artefacts. These strong artefacts have the common feature that the correlating forward and backward wavefields propagate in almost the opposite direction to each other at each correlation point. This is because the ray paths of the forward and backward wavefields are almost identical. In this paper, we present several tactics to avoid artefacts in shot-domain reverse-time migration. Simple muting of a shot gather before migration, or wavefront migration which performs correlation only within a time window following first arriving travel times, are useful in suppressing artefacts. Calculating the wave propagation direction from the Poynting vector gives rise to a new imaging condition, which can eliminate strong artefacts and can produce common image gathers in the reflection angle domain.

## INTRODUCTION

Wave equation migration correctly handles both multi-path arrivals and the phase changes due to caustics. RTM (Reverse-time migration), which propagates the source wavefield forward and the measured wavefield backward in time using the hyperbolic wave equation, does not suffer from the dip limitation of one-way downward-continuation algorithms (Hemon, 1978; Baysal et al., 1983; Whitmore, 1983; McMechan, 1983). Numerical solution of the hyperbolic wave equation for large, real 3D problems is expensive and not easy to compute on PC-based Linux cluster platforms. However, this is no longer an unsurmountable obstacle, due to rapid developments in computer hardware. Moreover, developments such as high-order finite-difference schemes, variable grids (Mufti et al., 1996; Wu et al., 1996) and the pseudo-spectral method (Kosloff and Baysal, 1982; Fornberg, 1987) can reduce memory and disk requirements in RTM (Yoon et al., 2003). In velocity-model building procedures, especially for complex structures including salt bodies, RTM can be used as

an attractive tool with which to build consistent velocity models and final prestack depth migration images, with the ability to image turning waves and multi-path arrivals properly. With the help of wave-propagation movies and forward-modelled synthetic data obtained as by-products in RTM, we can further understand imaging problems and build more reliable velocity models.

The imaging condition of zero-lag cross correlation between forward- and backward-propagated numerical solutions of the hyperbolic wave equation gives rise not only to subsurface images, but also to artefacts harmful to those images. We will address several artefacts generated in shot-domain prestack depth RTM, and methods to remove such artefacts.

Source wavefields with large incident angles are refracted or propagated almost horizontally in the shallow subsurface, and are recorded principally as strong early arrivals at far-offset receivers. When wavefields that have been recorded as strong early arrivals at far offset propagate backward in time, they pass through the same ray path as forward-propagating source wavefields pass through, and result in strong artefacts at shallow depth by cross-correlating with forward wavefields. These artefacts, which are generated in shot-domain RTM, can be eliminated by excluding strong early arrivals at far offset before migration. We may use first-arriving travel times and define a time window that follows those travel times, and restrict correlation only to within the window. This wavefront migration can avoid to some extent correlating with forward wavefields which are back-scattered from a strong velocity contrast.

These artefacts arise when one wavefield correlates with another which is propagating from almost the opposite direction. On the other hand, reflection events we want to image are produced when forward and backward wavefields are correlated with narrow opening angles. Using the fact that reflection events and artefacts have different ranges of opening angle, we may use wave-propagation directions to eliminate artefacts. The Poynting vector gives a mathematical basis for computation of wave-propagation directions.

## Artefacts arising from the RTM imaging condition

RTM conventionally uses the well-established imaging condition of zero-lag cross correlation between the forward-propagated source wavefield and the backward-propagated measured wavefield. This imaging condition can be expressed as

$$I(x, y, z) = \int_0^{t_{\max}} S(x, y, z, t) R(x, y, z, t) dt \quad (1)$$

where  $I(x, y, z)$  is the depth image,  $S(x, y, z, t)$  and  $R(x, y, z, t)$  are the forward-propagating source wavefield and backward-propagating receiver wavefield and  $t_{\max}$  is the recording time. RTM enables us to image turning waves which are reflected from reflectors whose dips exceed 90° because it uses numerical solution of the full wave equation. The same capability that allows us to image turning waves also results in spurious cross-correlation with head waves, direct turning waves, and back-scattered waves, giving rise to

<sup>1</sup> School of Civil, Urban and Geosystem Engineering,  
Seoul National University,  
San 56-1, Sillim-dong, Gwanak-gu,  
Seoul 151-740, Korea  
Phone: 82-2-875-6292  
Fax: 82-2-875-6296  
Email: ykwangjin@yahoo.co.kr

<sup>2</sup> Allied Geophysical Laboratories, University of Houston,  
4800 Calhoun Rd., Houston,  
Texas 77205, U.S.A.

Manuscript received 18 July, 2005.

Revised manuscript received 20 October, 2005.

artefacts. These artefacts are most noticeable at shallow depth.

Figure 1(a) is a 1D velocity model whose velocity increases at a constant gradient of 0.7 km/s and has a reflector arising from a velocity contrast of 0.5 km/s at depth  $z = 1.5$  km. Figure 1(b) is a shot profile for a source located at distance  $x = 3$  km. Figure 2(a) is an RTM image of the shot profile in Figure 1(b). Figure 2(a) shows an image severely contaminated with artefacts due to diving waves. Strong early arrivals recorded at far offset come from head waves and direct turning waves. These strong early arrivals dive into subsurface with large incidence angles and back-propagate to the source point. A backward-propagating diving wave produces low wavenumber artefacts by cross-correlating with the forward-propagating version of itself at nearly all points along its ray path. This low wavenumber smear is most troublesome on common-shot

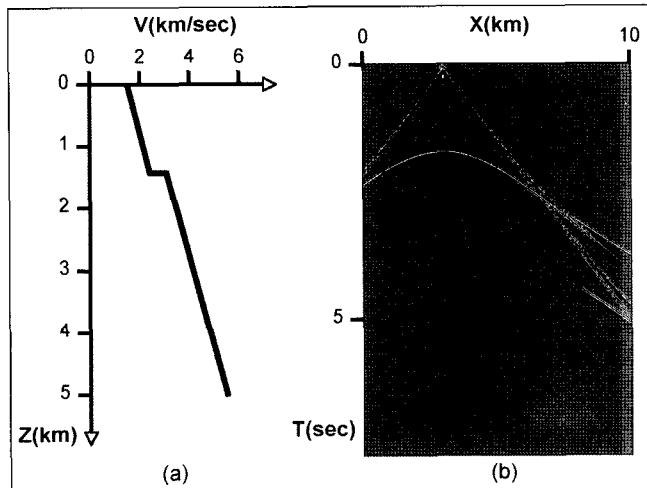


Fig. 1. a) 1D Velocity model for forward modelling. Velocity is determined by the relation  $v(z) = 1.5 + 0.7 \times z$ , where  $z$  is depth. There is a reflector with a velocity step of 0.5 km/s at 1.5 km depth. b) Synthetic shot profile for a source at  $x = 3$  km. Direct turning waves, refracted waves and multiples are dominant at far offset.

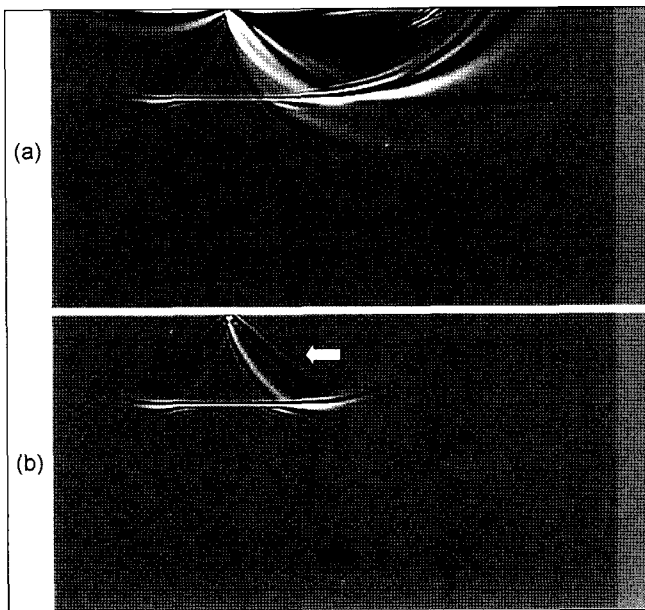


Fig. 2. RTM images of the shot profile given in Figure 1(b), (a) before muting and (b) after muting with  $v = 1.5$  km/s. The image without muting is severely contaminated with artefacts due to the direct turning waves and refracted waves recorded at far offset. The image after muting shows that muting efficiently eliminates these kinds of artefacts. However, artefacts due to back-scattered waves (white arrow) still remain above the reflector in (b). The artefact indicated by a black arrow originates from a multiple.

images which are needed for velocity analysis. Bandpass filtering can be applied to the stacked image (Mulder and Plessix, 2003), but the wavenumber of the noise is not so low as to be separated from reflection events with ease. Muting before back propagation is an efficient way to remove this artefact. Figure 2(b) is the RTM image when the shot-profile in Figure 1(b) is muted by a constant velocity  $v = 1.5$  km/s. We can see that the low wavenumber artefact has been removed properly. However, too much mute may remove signals that may be imaged as reflectors when they are correlated with forward wavefields.

This sweeping low wavenumber artefact is severe especially for models in which velocity increases smoothly with depth. Figure 3(a) and 3(b) show RTM images of a marine shot profile where a smoothly increasing background velocity has been used as the migration velocity. In Figure 3(a), the RTM image of the raw data, a sweeping artefact overwhelms the subsurface image, especially at shallow depths. The amplitude of the artefact decreases with depth while its wavenumber increases up to approximately the same wavenumber as the reflection image. In Figure 3(b), an RTM image of the data muted with  $v = 1.2$  km/s, we can see that artefacts are removed well and images are preserved properly.

Another artefact arises when source and receiver wavefields propagate through a heterogeneous medium, especially where waves meet a strong velocity contrast such as a salt boundary. Figure 4(a) is the RTM image of a shot profile from the Sigsbee2a data set. While impedance matching, which sets  $\rho v$  (density  $\times$  velocity) as a constant, helps to avoid back-scattering wavefields when they hit an interface at near normal incidence (Baysal et al., 1984), the interface still backscatters significant energy at large incidence angles. Figure 4(b) is the image using the impedance matching technique. It shows that the impedance matching technique is not useful in the shot domain. Furthermore, in order to consider not only velocity but also density, we must pay double to compute additional first derivatives of the wavefield.

The artefact above the salt is produced when the forward-propagating source wavefield correlates with the wavefield backward propagated and backscattered from the salt, or vice versa. To remove this noise, we need to suppress both backscattered wavefields. While it is now known to be inadequate for imaging beneath complex structures, first-arrival Kirchhoff migration is still a reasonably accurate tool for imaging many geological

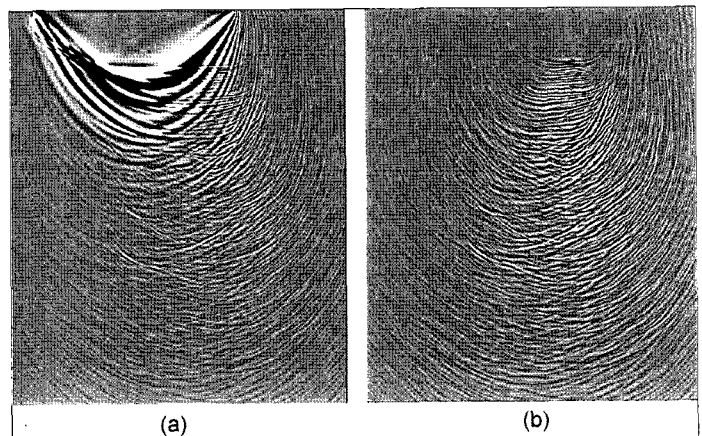


Fig. 3. RTM image of a marine shot profile (a) before muting and (b) after muting with  $v = 1.2$  km/s. A smoothly increasing velocity is used as the migration velocity. Simple muting has eliminated the artefact properly. However, too much muting may also eliminate the reflection image, and a high-wavenumber artefact may remain because its wavenumber  $k_z$  is too high to be separated with ease.

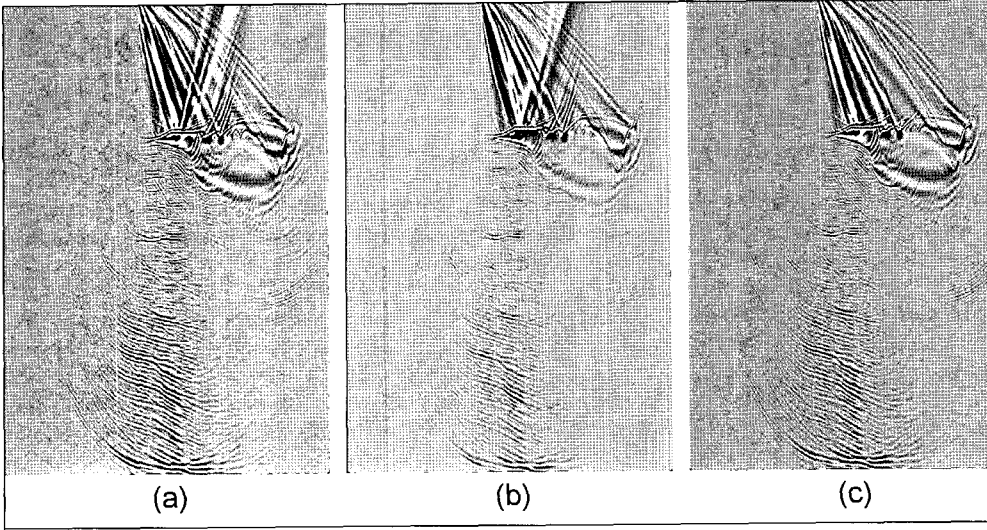


Fig. 4. RTM images showing artefacts due to wavefields back-scattered from a strong velocity contrast. RTM images obtained by a) conventional imaging condition that correlates source and measured waves at whole subsurface imaging points as shown in equation (3); b) conventional imaging condition with impedance matching, which fixes  $\rho v$  as a constant; and c) windowed cross-correlation, which does correlation only within a time window following the first arrivals. Impedance matching is not useful in suppressing back-scattering waves in the shot domain. Windowed cross-correlation can eliminate the back-scattering source wave.

terraces. We also note that the more accurate, most energetic or shortest-path arrivals arrive at times that are reasonably close (say within 500 ms) to the first arrival. Energy arriving much later than 500 ms behind the first arrival is increasingly sensitive to our inaccurate velocity model, which further increases the chance of spurious correlation with valid scattered energy from other parts of the model. Thus, we can follow Zhou and Schuster (2002) and use only cross-correlated events at times following a finite time behind the source field wavefront. Figure 4(c) shows the image using windowed cross-correlation. We used first-arriving and most energetic travel times, picked during source wavefield forward propagation. Source wavefields outside the window were set to zero before correlation with back-propagated wavefields. By suppressing source wavefield back-scattering from the salt, we can remove the noise generated from the cross-correlation of upgoing back-scattered source wavefield with the downgoing measured wavefield, as shown in Figure 4(c).

### AN IMAGING CONDITION USING POYNTING VECTORS

We have addressed artefacts arising from diving waves and back-scattered wavefields. These artefacts have the common feature that one wave correlates with another wave propagating in just the opposite direction. If the velocity model is correct, it is natural that all back-propagated measured wavefields will collapse into the source point and correlate with the source wavefield, although they experience various phenomena, such as reflection, refraction, scattering, and so on. While muting and windowed cross-correlation is useful in suppressing these noises, to obtain a more general method, we need a new imaging condition that excludes correlation between waves that propagate in opposite directions. The Poynting vector, a measure of energy flow, provides us with the mathematical tool needed to compute wave propagation direction. Wave propagation direction enables us to differentiate between events that travel in the same direction and are in phase at a scattering point from those events that travel in opposite directions and are in phase along long parts of their travel path. Two wavefields that correlated with each other and result in a reflection event propagate in similar directions, with a narrow opening angle at the imaging point. On the other hand, head waves, diving waves, undesired reverberations at large angles of incidence at velocity heterogeneities, and back scattered waves produce artefacts when they correlate with the other forward or backward wave field, which propagates in almost the opposite direction at an imaging point.

From staggered grid algorithms or additional computations, we

can calculate both pressure  $P$  and its spatial first derivatives  $dP/dx$ ,  $dP/dy$ , and  $dP/dz$ . Then the ray direction vector  $\mathbf{v}$  can be computed by multiplying  $-dP/dt$  by the particle movement vector  $(dP/dx, dP/dy, dP/dz)$ . The Poynting vector is proportional to  $-\mathbf{v}P$ . It can be expressed as

$$\text{Poynting vector} \equiv -\mathbf{v}P = -\nabla P \frac{dP}{dt} P \quad (2)$$

Instead of forming the imaging condition:

$$I = \frac{\sum_s P_s(t) P_g(t)}{\sum_s [P_s(t)]^2} \quad (3)$$

where  $P_s(t)$  and  $P_g(t)$  are pressures in the source and receiver wavefields respectively, which equally weights correlations of energy crossing in any direction, we can design a filter that uses the direction of energy transport. In particular, we would like to accept the correlation of backwards-propagated energy that is aligned to within say,  $120^\circ$ , of the forward-propagated source Poynting vector, and attenuate backwards-propagating energy that is aligned between  $120^\circ$  and  $180^\circ$  of the source Poynting vector. We can make a weighting table  $W(\cos \theta)$  depending on the opening angle between two correlating waves from the relation

$$\cos \theta = \frac{\mathbf{v}_s(t) P_s(t) \cdot \mathbf{v}_g(t) P_g(t)}{|\mathbf{v}_s(t) P_s(t)| |\mathbf{v}_g(t) P_g(t)|} \quad (4)$$

Then the new imaging condition becomes

$$I = \frac{\sum_s [P_s(t) P_g(t) W(\cos \theta)]}{\sum_s [P_s(t)]^2} \quad (5)$$

If we want to exclude the correlation whose opening angle exceeds  $120^\circ$ ,  $W(\cos \theta)$  may be set to 1 where  $\cos \theta \geq -0.5$ , and 0 elsewhere.

Figures 5 and 6 show snapshots and the corresponding ray direction vectors  $\mathbf{v}$ . Figure 5(a) and Figure 6(a) are snapshots of forward and backward propagating wavefields at every 0.5 seconds. Figures 5(b) and 5(c) are the  $x$  and  $z$  components of  $\mathbf{v}_s$ , the ray direction vector of the source wavefield. Figures 6(b) and 6(c) are the  $x$  and  $z$  components of  $\mathbf{v}_g$ , the ray direction vector of the

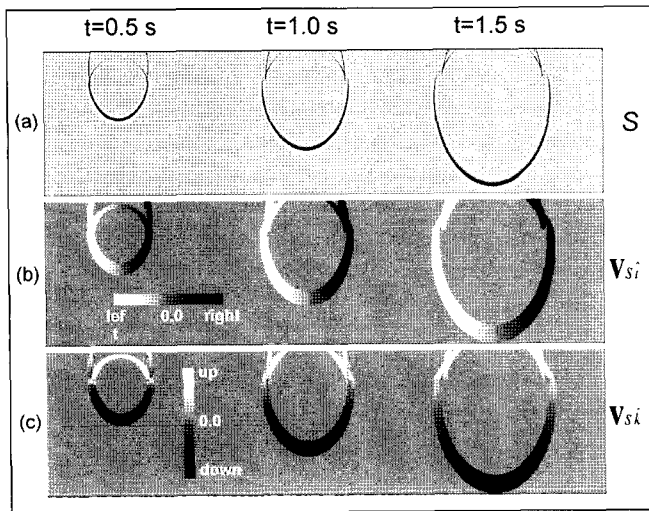


Fig. 5. a) source wavefield snapshots at every 0.5 second; b) horizontal; and c) vertical component of the source wavefield Poynting vector at each time frame. In Figures 5(b) and 5(c), white and black colours mean negative and positive directions, respectively.

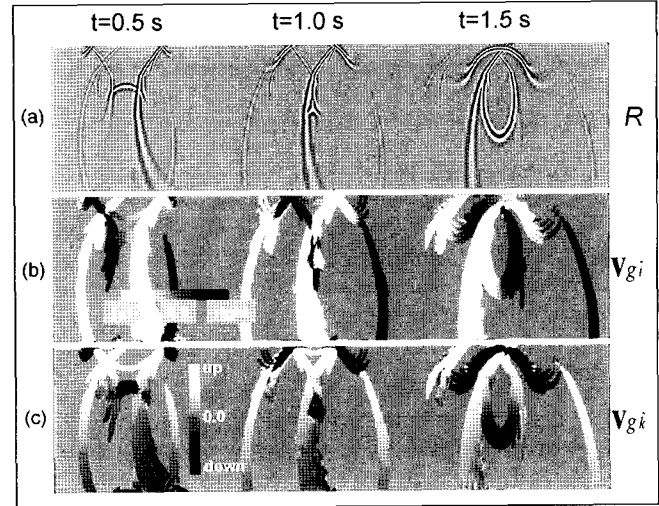


Fig. 6. a) back-propagated measured wavefield snapshots at every 0.5 second; b) horizontal; and c) vertical component of the measured wavefield Poynting vector at each time frame. In Figures 6(b) and 6(c), white and black colours mean negative and positive directions, respectively.

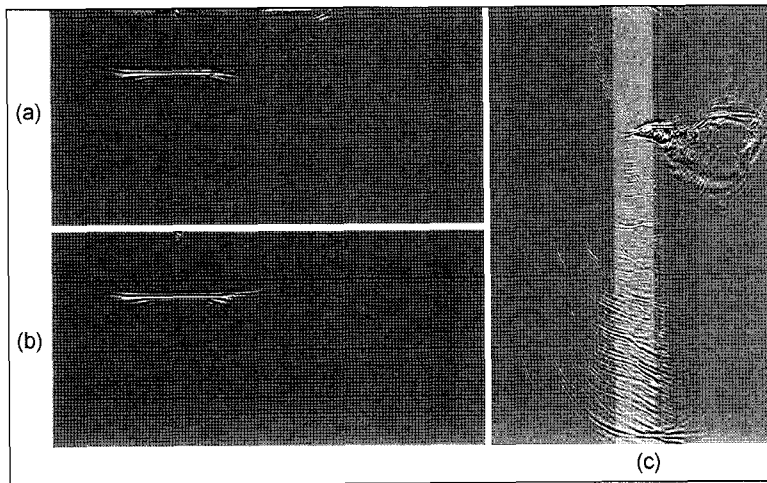
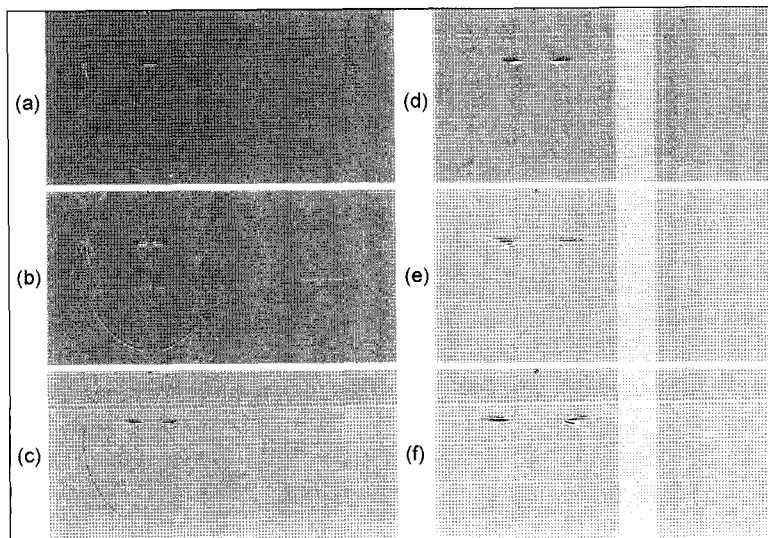


Fig. 7. RTM images obtained by using the imaging condition in equation (5) to exclude cross-correlations whose opening angles are greater than  $120^\circ$ . Panels (a), (b), and (c) correspond to Figures 2(a), 2(b), and 4(a), which are RTM images using the imaging condition in equation (3).



measured backward-propagating wavefield. Black colour denotes positive  $x$  and  $z$  directions, while white colour denotes negative  $x$  and  $z$  directions. Figure 7 shows RTM images using the imaging condition in equation (5) with the weight 1 when the opening angle is less than  $120^\circ$ . Figures 7(a), 7(b), and 7(c) correspond to Figures 2(a), 2(b), and 4(a), which are RTM images obtained by applying the imaging condition in equation (3). We can see that the imaging condition in equation (5) has removed artefacts originated from diving and refraction waves (Figure 7(a) and 7(b)) and back-scattered waves (Figure 7(c)) properly.

In wave-equation shot-profile migration including RTM, we can obtain angle domain common image gathers (ADCIGs) after migration by transforming offset domain common image gathers (ODCIGs) which are computed during migration (Rickett and Sava, 2002; Sava and Fomel, 2003). In RTM, we may extract ADCIGs during migration directly from opening angles and correlated values calculated at common image points with negligible additional computation and storage. Figure 8 shows RTM images at different reflection angle ranges. Figures 8(a), 8(b), 8(c), 8(d), 8(e), and 8(f) are images of a shot-profile whose incident angles are within the range of  $0^\circ\sim 10^\circ$ ,  $10^\circ\sim 20^\circ$ ,  $20^\circ\sim 30^\circ$ ,  $30^\circ\sim 40^\circ$ ,  $40^\circ\sim 50^\circ$ , and  $50^\circ\sim 60^\circ$ , respectively.

## CONCLUSION

RTM can handle multi-path arrivals and turning waves properly. It also helps us to further understand imaging problems and to build more reliable velocity models with forward modelling capability. When RTM images suffer from artefacts originating from diving waves or backscattered waves, we can improve image quality by

Fig. 8. RTM images whose incident angle is within the range of (a)  $0^\circ\sim 10^\circ$ , (b)  $10^\circ\sim 20^\circ$ , (c)  $20^\circ\sim 30^\circ$ , (d)  $30^\circ\sim 40^\circ$ , (e)  $40^\circ\sim 50^\circ$ , and (f)  $50^\circ\sim 60^\circ$ . Figure 7(b) is the image whose incident angle is within the range of  $0^\circ\sim 60^\circ$ .

applying simple muting, by using windowed cross-correlation, or by using an imaging condition that considers wave propagation directions. With the help of the Poynting vector, we can extract ADCIGs during RTM and obtain shot domain images of various reflection angle ranges.

## ACKNOWLEDGMENTS

We thank the Subsalt Multiples Attenuation and Reduction Technology Joint Venture (SMAART JV) for providing the Sigsbee2a data set and velocity model. We thank Lindsay Thomas at the University of Melbourne for his careful edit.

## REFERENCES

- Baysal, E., Kosloff, D.D., and Sherwood, J.W.C., 1983, Reverse-time migration: *Geophysics*, **48**, 1514–1524.
- Baysal, E., Kosloff, D.D. and Sherwood, J.W.C., 1984, A two-way nonreflecting wave equation: *Geophysics*, **49**, 132–141.
- Fornberg, B., 1987, The pseudo-spectral method: Comparisons with finite difference for the elastic wave equation: *Geophysics*, **52**, 483–501.
- Hemon, c., 1978, Equations d'onde et modeles: *Geophysical Prospecting*, **26**, 790–821.
- Kosloff, D.D., and Baysal, E., 1982, Forward modelling by a Fourier method: *Geophysics*, **47**, 1402–1412.
- McMechan, G.A., 1983, Migration by extrapolation of time-dependent boundary values: *Geophysical Prospecting*, **31**, 413–420.
- Mufti, I.R., Pita J.A., and Huntley, R.W., 1996, Finite-difference depth migration of exploration-scale 3-D seismic data: *Geophysics*, **61**, 776–794.
- Mulder, W., and Plessix, R., 2003, One-way and two-way wave-equation migration: *73rd Annual International Meeting and Exhibition, Society of Exploration Geophysicists, Expanded Abstracts*, 881–884.
- Rickett, J. and Sava, P., 2002, Offset and angle-domain common image-point gathers for shot-profile migration: *Geophysics*, **67**, 883–889.
- Sava, P. and Fomel, S., 2003, Angle-domain common-image gathers by wavefield continuation methods: *Geophysics*, **68**, 1065–1074.
- Whitmore, N.D., 1983, Iterative depth imaging by backward time propagation: *53rd Annual International Meeting and Exhibition, Society of Exploration Geophysicists, Expanded Abstracts*, 382–384.
- Wu, W., Lines, L.R., and Lu, H., 1996, Analysis of higher-order, finite-difference schemes in 3-D reverse-time migration: *Geophysics*, **61**, 845–856.
- Yoon, K., Shin, C., Suh, S., Lines, L.R., and Hong S., 2003, 3D reverse-time migration using acoustic wave equation: An experience with the SEG/EAGE data set: *The Leading Edge*, **22**, 38–41.
- Zhou, M. and Schuster, G., 2002, Wave-equation wavefront migration: *72nd Annual International Meeting and Exhibition, Society of Exploration Geophysicists, Expanded Abstracts*, 1292–1295.

## 포인팅 벡터를 이용한 역시간 구조보정

윤광진<sup>1</sup>, Kurt J. Marfurt<sup>2</sup>

**요약:** 최근 급속히 발전하는 하드웨어로 인해 역시간 구조보정을 다양한 현장자료의 영상화에 적용할 수 있게 되었다. 양방향 파동방정식을 이용하는 파동방정식 구조보정 방법으로, 역시간 구조보정은 다중 도달과 뿐 아니라 급경사 및 수직 이상의 경사를 갖는 반사면도 영상화가 가능하다. 그러나 쌍곡선 파동방정식의 양방향 전파라는 성질로 인해 역시간 구조보정은 잡음을 발생시킨다. 연속적으로 입사각이 증가하여 지표로 전파되는 파, 선두 파, 역 산란 파 등과의 영 지연 상호상관은 의사영상을 만든다. 이러한 큰 진폭의 의사영상은, 상호상관되는 각 점에서 볼 때, 순 전파 및 역 전파되는 두 파동장들이 거의 정 반대방향으로 전파한다는 공통점을 갖고 있다. 이는 순 전파하는 파동장과 역 전파하는 파동장의 두 전파경로가 거의 일치함으로써 발생한다. 본 논문에서는 음원 모음 역시간 구조보정에서의 의사영상을 제거하는 몇 가지 시도들을 소개하고자 한다. 구조보정 전에 실시하는 음원모음자료의 간단한 뮤팅 또는 초동 주시 이후의 시간 창 이내에서만 상호상관을 실시하는 파면 구조보정은 이러한 의사영상을 제거하는데 효과적이다. 포인팅벡터로부터 계산한 파동방정식의 전파방향을 이용하면 큰 진폭의 의사영상을 제거할 수 있는 새로운 영상화 조건을 적용할 수 있고 반사각에 따른 공통영상모음을 구할 수 있다.

**주요어:** 파동방정식 구조보정, 역시간, 포인팅 벡터, 공통영상모음

## Poynting ベクトルを使ったリバースタイム・マイグレーション

尹 光鎮(윤 쿄운진)<sup>1</sup>・カート J. マルフート<sup>2</sup>

**要旨:** 最近、コンピュータ・ハードウェアの急速な発達によって、多くの実データを用いた(プロダクションの)イメージングの問題にリバースタイム・マイグレーションの適用が可能になった。リバースタイム・マイグレーションは往復の波動方程式を使用するので、多経路から到着する反射波だけではなく、急傾斜からの反射波や、経路が大きく曲がる反射波等も取り扱うことができる。しかし、リバースタイム・マイグレーションは双曲線波動方程式が往復経路を用いている事に起因する、望ましくない偽像を作り出す事がある。ダイビングウェーブ、ヘッドウェーブ、および後方散乱波などのゼロラグ相互相関がこうした偽像を起こす。強い偽像を発生させるこれらのイベントは、それぞれの相関点で前方・後方進行波がお互いほとんど逆方向に伝播するという共通点を持っている。これは前方・後方進行波の波動経路がほとんど同じだからである。この論文では著者らは、ショット記録を用いたリバースタイム・マイグレーションの偽像を避けるためのいくつかの方法を提示する。マイグレーション以前のショットギャザーの単純なミュートや、初動走時後以後に設定した時間ウィンドウ内だけで相関を実行する波面マイグレーション、等は偽像の抑圧に役立つ。Poynting ベクトルから波動の伝播方向を計算すると、強い偽像を除去する事ができる新しいイメージング条件、および反射角領域での共通イメージギャザーを得る事ができる。

**キーワード:** 波動方程式マイグレーション、リバースタイム、Poynting ベクトル、共通イメージギャザー

<sup>1</sup> 서울대학교 공과대학 지구시스템공학부  
151-740 서울 관악구 신림동 산 56-1

<sup>2</sup> University of Houston, Center for Applied Geosciences and Energy

<sup>1</sup> ソウル大学校工科大学地球システム工学部

<sup>2</sup> ヒューストン大学 応用地球科学エネルギーセンター